

## Assessment of a fictitious domain method for patient-specific biomechanical modelling of press-fit orthopaedic implantation

L.F. Kallivokas<sup>a\*</sup>, S.-W. Na<sup>a</sup>, O. Ghattas<sup>b</sup> and B. Jaramaz<sup>c</sup>

<sup>a</sup>Department of Civil, Architectural and Environmental Engineering, The University of Texas at Austin, 1 University Station, C1748, Austin, TX 78712, USA; <sup>b</sup>The Institute for Computational Engineering and Sciences, The University of Texas at Austin, 1 University Station, C0200, Austin, TX 78712, USA; <sup>c</sup>Robotics Institute, Carnegie Mellon University, 5000 Forbes Avenue, Pittsburgh, PA 15213, USA

(Received 24 June 2010; final version received 3 December 2010)

In this article, we discuss an application of a fictitious domain method to the numerical simulation of the mechanical process induced by press-fitting cementless femoral implants in total hip replacement surgeries. Here, the primary goal is to demonstrate the feasibility of the method and its advantages over competing numerical methods for a wide range of applications for which the primary input originates from computed tomography-, magnetic resonance imaging- or other regular-grid medical imaging data. For this class of problems, the fictitious domain method is a natural choice, because it avoids the segmentation, surface reconstruction and meshing phases required by unstructured geometry-conforming simulation methods. We consider the implantation of a press-fit femoral artificial prosthesis as a prototype problem for sketching the application path of the methodology. Of concern is the assessment of the robustness and speed of the methodology, for both factors are critical if one were to consider patient-specific modelling. To this end, we report numerical results that exhibit optimal convergence rates and thus shed a favourable light on the approach.

**Keywords:** fictitious domain method; regular and geometry-conforming finite element methods; press-fit implant; linear elasticity; CT- or MRI-scan; medical imaging

### 1. Introduction

Today, in total hip replacement surgeries, typical pre-operative planning systems are based on geometric templating capabilities that, invariably, are used to find an appropriate match between the femoral and acetabular implants and their respective receiving bony structures (e.g. Figure 1). Femoral implant choices can be roughly classified into cementless and cemented: the latter refers to femoral implants whose bonding to the receiving femoral canal is ascertained via a bonding agent ‘cement’, whereas the former refers to bonding ascertained via press-fitting an over-sized implant. In either case, the primary intent is to allow for an as-normal-as-possible post-operative range of motion as the healthy anatomy would have provided. Here, the focus is on cementless implants: for these, by and large, it is the anatomical geometry, coupled with the experience of the operating surgeon, that dictates the implant choice, without the desirable benefit of an *a priori* estimate of the stresses induced to the bones due to such a choice.

If, however, a biomechanical feedback mechanism were to exist that would present, in a way meaningful to the planning surgeon, the potential mechanical effects of a specific implant choice, it is then conceivable that such a mechanism would act as a safety feature (Krejčí et al.

1997). Its introduction might prevent selections leading to either short- or long-term failures of the chosen implant, and thus to a potential improvement of the clinical outcome.<sup>1</sup> The introduction of robotic systems into the operating room (Kanade et al. 1996) – responsible for preparing the femoral cavity receiving the implant – only accentuated the need for pre-operative planners enhanced with such a biomechanical feedback mechanism. However, the inclusion of a feedback module into a pre-operative system imposes severe demands for computational speed and robustness of the underlying geometry and analysis modelling tools, especially if one were to consider the onerous requirements of patient-specific modelling. It is within the above framework that we explore in this article the applicability and suitability of a fictitious domain method as part of an analysis tool of a biomechanical feedback mechanism for a pre-operative surgical planner.

A first step in any attempt to address the mechanical (e.g. stress) effects of the implantation process has perforce to start from the reconstruction of the femoral geometry. Thus, one strategy for patient-specific geometric modelling is to develop solid models of bone volumes by reconstructing computed tomography (CT) data, and then use these models to generate physical

\*Corresponding author. Email: loukas@mail.utexas.edu

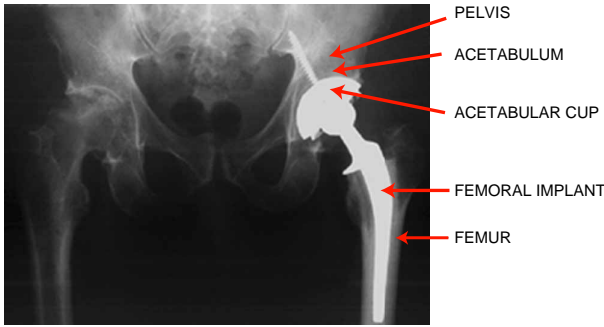


Figure 1. Typical post-operative total hip replacement X-ray; shown are the patient's acetabulum, femur, acetabular cup and femoral implant.

models appropriate for simulation (e.g. using finite element meshes within the encompassed volumes). The steps to such a process are pictorially depicted in Figure 2. Invariably one starts from slices of the anatomical geometry obtained using patient CT-scans that result in a series of planar tomographic images. Next, the collected

images undergo noise-filtering to remove artefacts. Extraction of bony boundaries (segmentation) is accomplished by edge detection algorithms, often based on density threshold values, yielding contours on each tomographic cross section which typically separate the cortical (hard) from the cancellous (spongy) bone (red rectangle A in Figure 2). Having identified the bony geometry on the planar slices, the next step involves the reconstruction of the three-dimensional anatomy (surface reconstruction step; blue rectangle B in Figure 2) by connecting the contours extracted in the previous step (often achieved via triangulation). Once the 3D reconstruction has been completed, one also needs to identify the femoral canal volume (receiving the implant), the surrounding bony volume, while also simulating the femoral neck osteotomy that will result in a modified solid model volume (rectangle C (green) in Figure 2). The insertion of the implant (selection is made pre-operatively, and a solid model for the implant is constructed as per the rectangle D (black) in Figure 2) will result in the intersection of the bone volumes identified in the previous

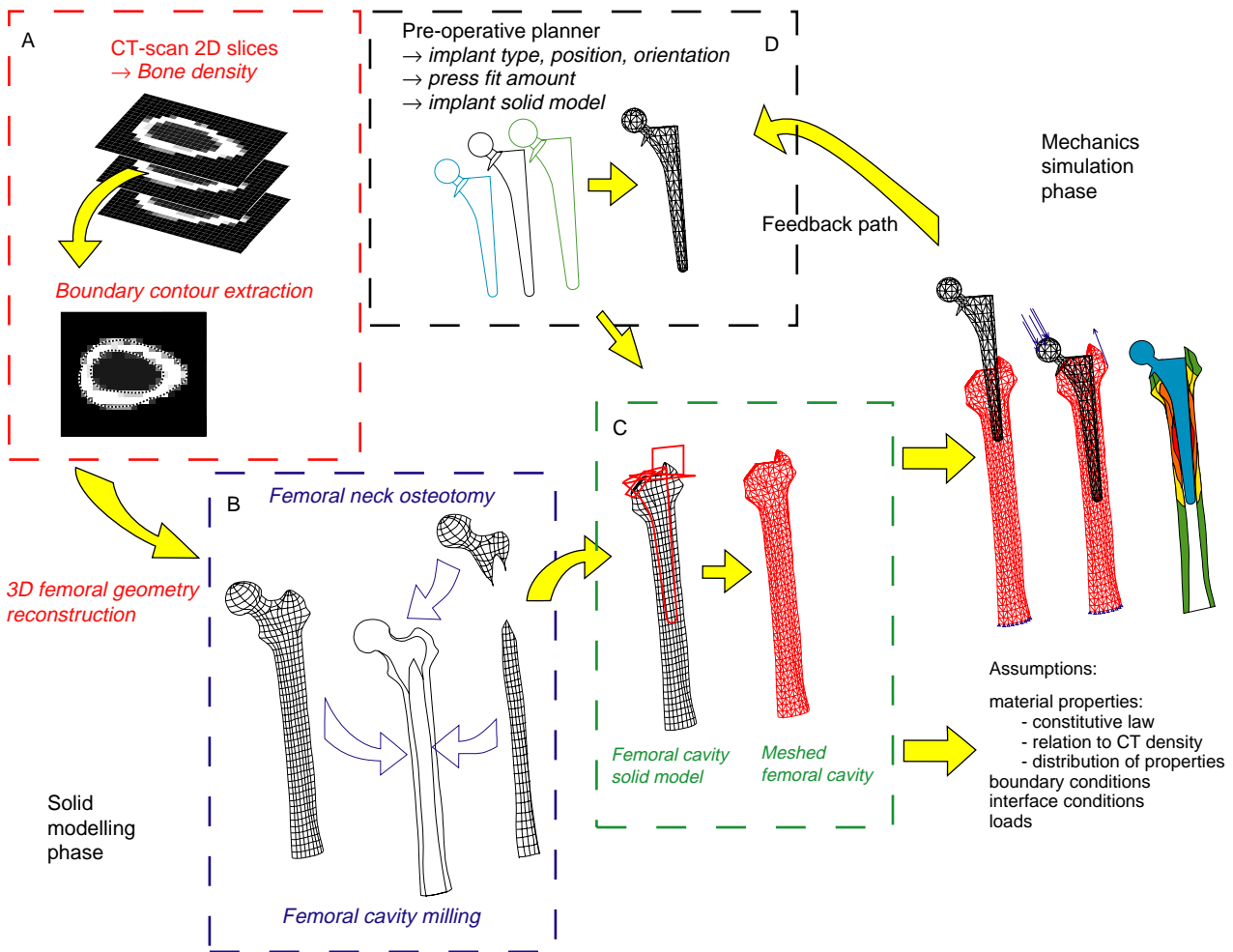


Figure 2. Typical modelling sequence based on unstructured meshes.

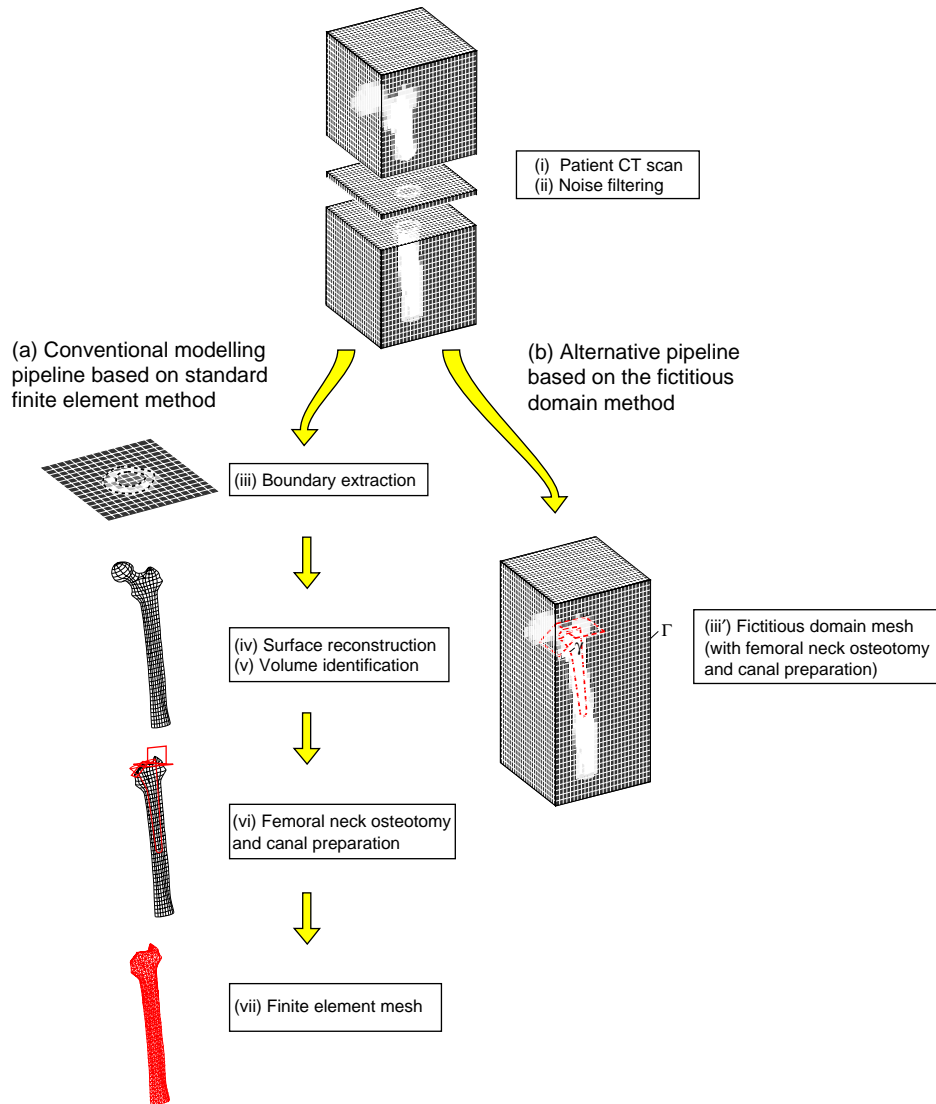


Figure 3. Modelling sequence based on conventional finite element meshes vs. regular grids (fictitious domain).

step, leading to the final solid model. The last step, following a conventional finite element modelling approach, involves the meshing of the final solid model and, given loads, material properties and boundary conditions, the subsequent simulation of the press-fit problem.

The process described thus far is an exacting one, plagued also by uncertainty with respect to whether the underlying algorithms could always deliver a final solid model – a hard requirement for patient-specific modelling: for example, the 3D surface reconstruction step from the planar slices may not always admit a unique solution. More importantly though, there are many sources of error introduced at every step of the outlined process: these include CT imaging errors, boundary extraction errors, surface generation errors and meshing errors. Furthermore, the surface reconstruction and the intersection of volumes

during the insertion of the implant (neck osteotomy and canal preparation) result in geometrically complex volumes, characterised by fine geometric features, that are difficult to mesh using unstructured techniques, if at all possible (fine features typically drive, at least locally, 3D meshes), given a reasonable set of computational resources – both hardware and software.

We remark that in this process, the CT-scan data are perforce considered as the best anatomical information that is available for modelling – a sort of a ground truth. The approximation errors that are introduced during the outlined modelling path, and prior to the simulation, potentially distort that ground truth (Lengsfeld et al. 1998). Therefore, if one were to avoid the accumulation of these errors, while simultaneously resolving or sidestepping the meshing difficulties without sacrificing computational speed or accuracy, one would obtain a fast and robust

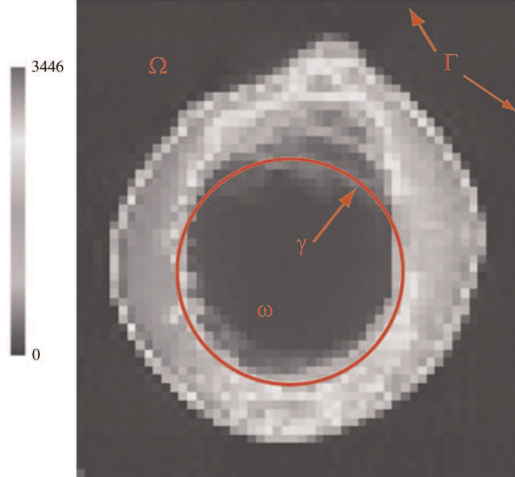


Figure 4. Typical grey-scale femoral cross-section CT-scan.

simulation tool capable of addressing the needs of patient-specific modelling. We turn to the *fictitious domain method* in search of such a tool and use Figure 3 to sketch the alternative modelling path.

Accordingly, we operate directly on the original 3D voxel data, without going through the steps of segmentation and 3D surface reconstruction. The boolean operations of the neck osteotomy and of the implantation are performed by imposing traction and displacement constraints on the surface ( $\gamma$ ) of the cutting planes and of the implant (assumed rigid), respectively (Figure 3). The solution for the stresses exterior to the implant surface and within the bony domain is obtained by direct application of the fictitious domain method on the original grid provided by the CT-scan. Thus, we summarily bypass all the geometric, image processing, solid modelling and meshing

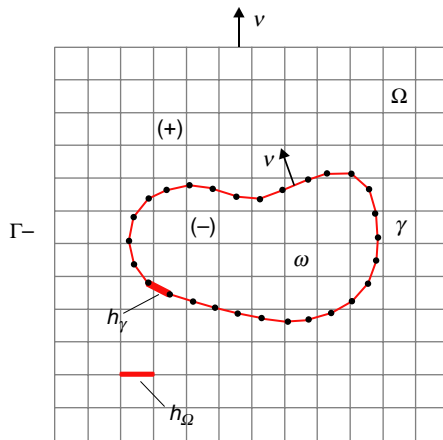


Figure 5. Regular grid (background) covering  $\Omega$  with mesh metric  $h_\Omega$ ; Dirichlet boundary grid (foreground)  $\gamma$  with mesh metric  $h_\gamma$ .

errors/difficulties outlined earlier. In the next sections, we provide the technical details.

## 2. Background

To fix ideas, we turn to the 2D counterpart of the problem described in Section 1: Figure 4 depicts a slice of a patient's femur, where the shades of grey in the pixels correspond to different bone densities. The circular inset (red) in Figure 4 represents the (cross-sectional) boundary of a rigid implant (assumed here to be of circular cross section) press-fitted into the femoral canal; the region  $\omega$  interior to the circular boundary  $\gamma$  is occupied, post-interventionally, by the metallic implant (not shown). Given a preset amount for the press-fit, and a material description afforded by the CT-scan, the goal is to determine the displacement and/or stress field in the exterior of the implant, i.e. within the affected part of the femur. We remark that the pixel data are provided, as it is typically the case, on a regular grid. Thus, as argued, the problem lends itself naturally to a fictitious domain formulation. Let  $\Omega$  denote the entire square 2D domain depicted in Figure 4 bounded by  $\Gamma$ ; let  $\omega$  denote the 'small' circular domain bounded by  $\gamma$  and fully embedded within  $\Omega$ . Let  $\mathbf{u}(\mathbf{x})$  denote the vector displacement field in  $\Omega \setminus \omega$ , i.e. exterior to  $\gamma$ ; we seek  $\mathbf{u}$  such that

$$\operatorname{div} \boldsymbol{\sigma} + \mathbf{f} = \mathbf{0}, \quad \text{in } \Omega \setminus \omega, \quad (1)$$

$$\mathbf{u} = \mathbf{g}, \quad \text{on } \gamma, \quad (2)$$

$$\boldsymbol{\sigma} \boldsymbol{\nu} = \mathbf{0}, \quad \text{on } \Gamma, \quad (3)$$

where customary notation has been used to denote the stress tensor  $\boldsymbol{\sigma}$ , the traction vector  $\boldsymbol{\sigma} \boldsymbol{\nu}$  on  $\Gamma$ , with  $\boldsymbol{\nu}$  the outward normal to  $\Gamma$ ;  $\mathbf{g}$  represents the Dirichlet datum on  $\gamma$  (press-fit amount) and  $\mathbf{f}$  denotes body forces. For the press-fit problem considered herein, there are no body forces, and thus  $\mathbf{f} = \mathbf{0}$ . We also note that the position of  $\Gamma$  is not critical to the underlying process, as long as  $\Gamma$  is exterior to any bone boundaries: this is always the case with properly collected CT-scans.

Under the simplifying assumption of linear elastic isotropic behaviour,<sup>2</sup> there also hold:

$$\boldsymbol{\sigma} = 2\mu \boldsymbol{\epsilon} + \lambda \mathbf{I} \operatorname{tr} \boldsymbol{\epsilon}, \quad (4)$$

$$\boldsymbol{\epsilon} = \frac{1}{2} (\nabla \mathbf{u} + \nabla \mathbf{u}^T), \quad (5)$$

where  $\boldsymbol{\epsilon}$  denotes the small-strain tensor,  $\mathbf{I}$  the second-order identity tensor, and  $\lambda$  and  $\mu$  are the Lamé constants.

Following classical lines of fictitious domain methods, the strong form (1)–(3), together with the constitutive relation (4) and the kinematic condition (5), can be recast

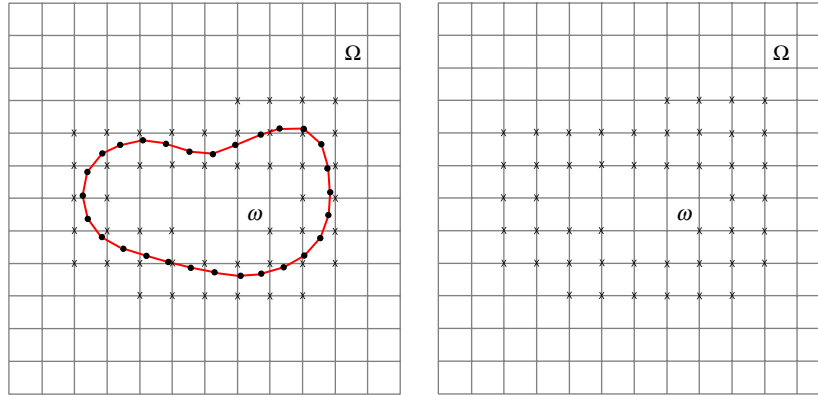


Figure 6. Schematic depiction of the role of  $\mathbf{B}$  matrix.

as: find  $\hat{\mathbf{u}}$  in  $\Omega$  such that

$$\operatorname{div} \hat{\boldsymbol{\sigma}} + \hat{\mathbf{f}} = \mathbf{0}, \quad \text{in } \Omega, \quad (6)$$

$$\hat{\mathbf{u}} = \mathbf{g}, \quad \text{on } \gamma, \quad (7)$$

$$\hat{\boldsymbol{\sigma}} \boldsymbol{\nu} = \mathbf{0}, \quad \text{on } \Gamma, \quad (8)$$

with

$$\hat{\boldsymbol{\sigma}} = 2\mu \hat{\boldsymbol{\epsilon}} + \lambda \mathbf{I} \operatorname{tr} \hat{\boldsymbol{\epsilon}}, \quad (9)$$

$$\hat{\boldsymbol{\epsilon}} = \frac{1}{2} (\nabla \hat{\mathbf{u}} + \nabla \hat{\mathbf{u}}^T), \quad (10)$$

where  $\hat{\mathbf{f}}$  represents an  $L_2$  extension of  $\mathbf{f}$  over the entire domain  $\Omega$ , such that the following restriction holds:

$$\hat{\mathbf{f}}|_{\Omega \setminus \omega} \equiv \mathbf{f}. \quad (11)$$

It can then be shown (e.g. Glowinski et al. 1994a) that the restriction of solution  $\hat{\mathbf{u}}$  over  $\Omega \setminus \omega$  coincides with the solution to the original problem defined only over the region exterior to  $\gamma$ , i.e.

$$\hat{\mathbf{u}}|_{\Omega \setminus \omega} \equiv \mathbf{u}|_{\Omega \setminus \omega}. \quad (12)$$

A statement similar to (12) can be written for  $\hat{\mathbf{u}}|_{\omega}$ , had the original problems (1)–(5) been cast over the domain  $\omega$  interior to  $\gamma$ . In fact, we will return to the interior problem in the next section. We remark that recasting the problem over the entire domain  $\Omega$  (as opposed to casting over the domain exterior to  $\gamma$  only), while weakly imposing the Dirichlet condition (7) on  $\gamma$ , offers the advantage of using a regular discretisation over  $\Omega$  (structured mesh), as opposed to an unstructured boundary-conforming mesh in  $\Omega \setminus \omega$ . In this way, we bypass the need for identifying material boundaries (they are implicit in the pixel data), by directly operating on the naturally regular grid provided by the CT-scan.

The weak imposition of the Dirichlet datum on  $\gamma$  via Lagrange multipliers gives rise to a saddle-point problem. The treatment of problems of this kind can be traced back to the 1960s in the (then) Soviet literature (e.g. Saul'ev 1963), where the term fictitious domain appears to have been coined for the first time. Later, Fix (1976) presented, under the heading of ‘hybrid’ finite element methods, one of the earliest discussions on how Dirichlet conditions can be imposed via Lagrange multipliers on interior boundaries embedded within a background grid. Other early developments can also be found in the (then) Soviet literature (see for example Astrakhansev 1978; Finogenov and Kuznetsov 1988). The theoretical underpinnings borrow largely from developments in mixed methods (Babuška 1973). A comprehensive review of fictitious domain methods, with many historical references, can be found in Glowinski (2003). Renewed interest in fictitious domain methods in the mid-1990s and later was fuelled (a) by the increasing need to solve 3D problems efficiently (3D unstructured quality meshing remains an open problem) and (b) by the maturation of fast solvers for

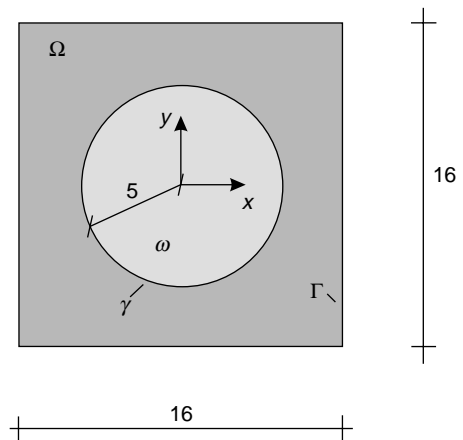


Figure 7. Domain for prototype Laplace problem.

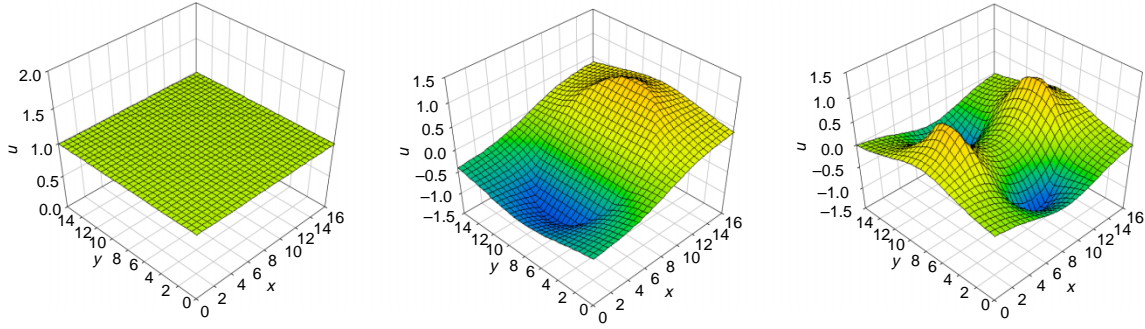


Figure 8. Exact solution  $\hat{u}$  (31) and (32) for  $n = 0, 1, 2$  (left to right) (Laplace prototype problem).

regular grid problems. Representative works include the many contributions of Glowinski and his collaborators on flows with rigid bodies (Glowinski et al. 1994b, 1997, 2001) and on other elliptic problems (Glowinski et al. 1996; Glowinski and Kuznetsov 1998; see also Maitre and Tomas 1999). Applications of the fictitious domain method now cover an ever-widening spectrum, including work on unsteady problems (Collino et al. 1997), fluid–structure interaction (Baaijens 2001), radiation and scattering problems for the Helmholtz operator (Heikkola et al. 1998, 2003; Nasir et al. 2003), the recent work on the treatment of the exterior Helmholtz problem by Farhat and Hetmaniuk (2002) and by Hetmaniuk and Farhat (2003a, 2003b), and the development of distributed forms of the fictitious domain method in which the constraints are imposed over regions as opposed to interfaces (Glowinski et al. 1998; Patankar et al. 2000). Applications to biomechanical problems are scantier (see De Hart et al. (2000, 2003), for modelling of the aortic valve), despite the attractiveness of the method for these problems. In this article, we build on past work (Shah et al. 1995; Kallivokas et al. 1996; Na et al. 2002) and discuss an application to linear elasticity of the fictitious domain method, also motivated by a biomechanics problem.

### 3. Mathematical formulation

We turn first to the interior problem (the counterpart to (1)–(5); Figure 5): find  $\mathbf{u}$  in  $\omega$  such that

$$\operatorname{div} \boldsymbol{\sigma} + \mathbf{q} = \mathbf{0}, \quad \text{in } \omega, \quad (13)$$

$$\mathbf{u} = \mathbf{g}, \quad \text{on } \gamma, \quad (14)$$

which, similarly to (6)–(10), is recast over the background domain  $\Omega$  as (henceforth, we use *background* to refer to  $\Omega$  and *foreground* to refer to  $\gamma$ ):

$$\operatorname{div} \hat{\boldsymbol{\sigma}} + \hat{\mathbf{q}} = \mathbf{0}, \quad \text{in } \Omega, \quad (15)$$

$$\hat{\mathbf{u}} = \mathbf{g}, \quad \text{on } \gamma, \quad (16)$$

$$\hat{\mathbf{t}} = \hat{\boldsymbol{\sigma}} \boldsymbol{\nu} = \mathbf{0}, \quad \text{on } \Gamma, \quad (17)$$

where  $\hat{\mathbf{q}}$  now represents an  $L_2$  extension of  $\mathbf{q}$  over the entire domain  $\Omega$ , such that the following restriction holds:

$$\hat{\mathbf{q}}|_{\omega} \equiv \mathbf{q}. \quad (18)$$

It can then be shown (Glowinski et al. 1994a) that the restriction of  $\hat{\mathbf{u}}$  in  $\omega$  is a solution of (13) and (14), i.e.  $\mathbf{u} = \hat{\mathbf{u}}|_{\omega}$ . Problems (15)–(17), together with (9) and (10), can be readily cast in a weak form: we multiply (15) by an admissible function  $\mathbf{v} \in H^1(\Omega)$ . There results:

$$\begin{aligned} \int_{\Omega} \mathbf{v} \cdot (\operatorname{div} \hat{\boldsymbol{\sigma}} + \hat{\mathbf{q}}) \, d\Omega &= \int_{\Omega \setminus \omega} \mathbf{v} \cdot (\operatorname{div} \hat{\boldsymbol{\sigma}} + \hat{\mathbf{q}}) \, d(\Omega \setminus \omega) \\ &+ \int_{\omega} \mathbf{v} \cdot (\operatorname{div} \hat{\boldsymbol{\sigma}} + \hat{\mathbf{q}}) \, d\omega \\ &= - \int_{\Omega} \hat{\boldsymbol{\sigma}} : \nabla \mathbf{v} \, d\Omega + \int_{\Gamma} \mathbf{v} \cdot \hat{\mathbf{t}} \, d\Gamma \quad (19) \\ &- \int_{\gamma} \mathbf{v} \cdot \hat{\mathbf{t}}^+ \, d\Gamma + \int_{\gamma} \mathbf{v} \cdot \hat{\mathbf{t}}^- \, d\Gamma \\ &+ \int_{\Omega} \mathbf{v} \cdot \hat{\mathbf{q}} \, d\Omega = 0, \end{aligned}$$

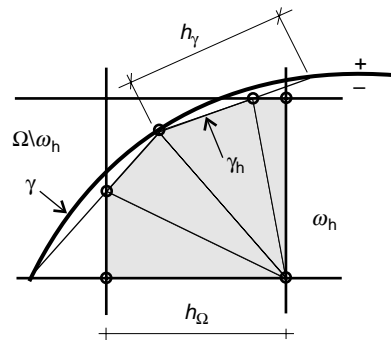


Figure 9. Typical boundary cell subdivision for error norm calculations.

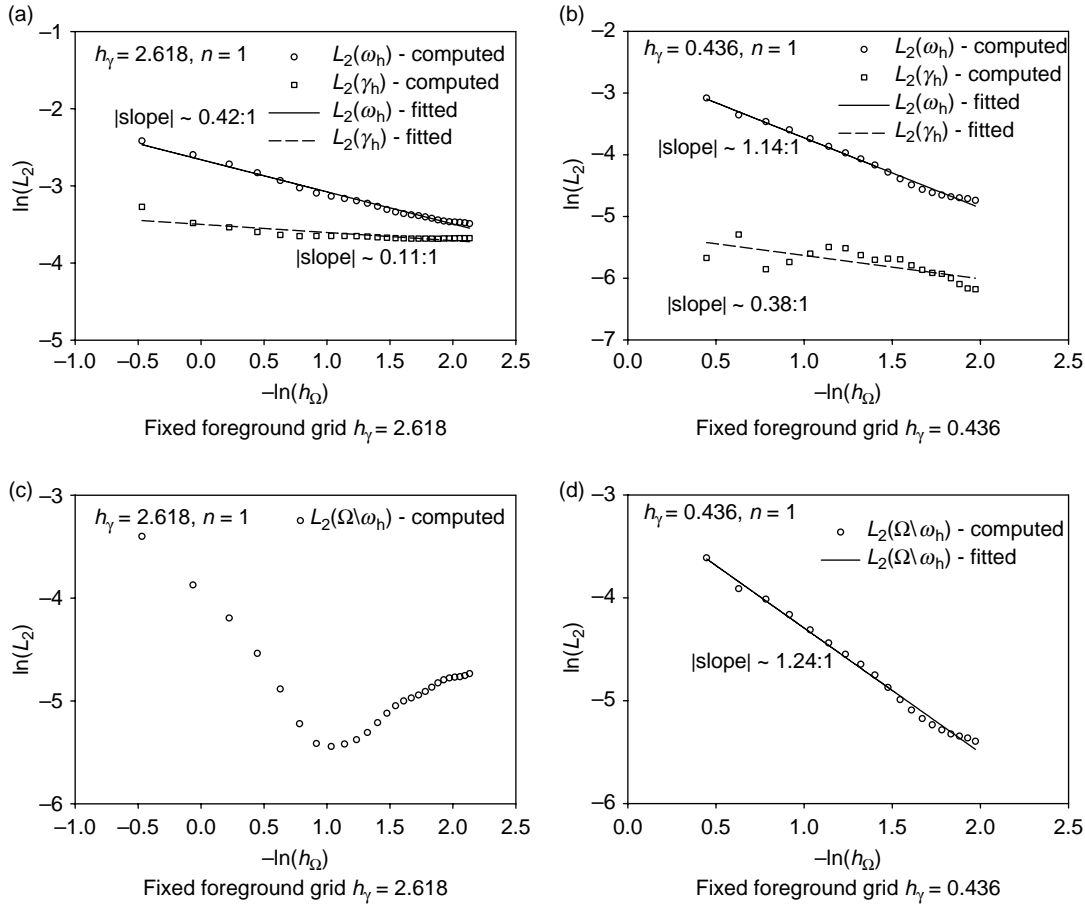


Figure 10. (a) and (b):  $L_2$  errors for  $\hat{u}$  in the interior  $\omega_h$  and on the boundary  $\gamma_h$ ; (c) and (d):  $L_2$  errors for  $\hat{u}$  in the exterior  $\Omega \setminus \omega_h$ ; one-sided refinement in  $h_\Omega$ , whereas  $h_\gamma$  is constant.

where  $\hat{\mathbf{t}}^-$  and  $\hat{\mathbf{t}}^+$  denote the boundary tractions on  $\gamma$ , computed from the interior ( $-$ ) and the exterior ( $+$ ) region to  $\gamma$ , respectively (Figure 5). Next, the Dirichlet condition (16) is imposed weakly on  $\gamma$  and, thus, we seek the pair  $(\hat{\mathbf{u}}, \hat{\boldsymbol{\xi}}) \in H^1(\Omega) \times H^{-(1/2)}(\gamma)$  such that:

$$\int_{\Omega} \hat{\boldsymbol{\sigma}} : \nabla \mathbf{v} \, d\Omega + \int_{\gamma} \hat{\boldsymbol{\xi}} \cdot \mathbf{v} \, d\gamma = \int_{\Omega} \hat{\mathbf{q}} \cdot \mathbf{v} \, d\Omega + \int_{\Gamma} \hat{\mathbf{t}} \cdot \mathbf{v} \, d\Gamma, \quad (20)$$

$$\int_{\gamma} \boldsymbol{\zeta} \cdot \hat{\mathbf{u}} \, d\gamma = \int_{\gamma} \boldsymbol{\zeta} \cdot \mathbf{g} \, d\gamma, \quad (21)$$

where, physically,  $\hat{\boldsymbol{\xi}}$  denotes the traction jump on the  $\gamma$  boundary, i.e.

$$\hat{\boldsymbol{\xi}} = [\hat{\mathbf{t}}^+ - \hat{\mathbf{t}}^-]. \quad (22)$$

The last term in (20) vanishes as per (17), and Equation (21) represents the weak imposition of the Dirichlet condition (16), where  $\boldsymbol{\zeta} \in H^{-(1/2)}(\gamma)$ . We remark that the same systems (20) and (21) could have been obtained by considering the Lagrangian of the problem and imposing

the Dirichlet condition via Lagrange multipliers  $\hat{\boldsymbol{\xi}}$ .<sup>3</sup> From (20) and (21), it also follows that one need only discretise the background domain  $\Omega$  and the boundary  $\gamma$  without resorting to (unstructured) discretisation that conforms to the boundary  $\gamma$ . In fact, the discretisations of  $\Omega$  and  $\gamma$ , from a geometrical point of view, are largely independent of each other (Figure 5). The approximations, though, for the pair of test functions  $(\mathbf{v}, \boldsymbol{\zeta})$  and the pair of trial functions  $(\hat{\mathbf{u}}, \hat{\boldsymbol{\xi}})$  cannot be independently chosen: due to the mixed nature of the problem (our unknowns are both the displacement vector and the (jump of the) tractions), the Ladyenskaja–Babuška–Brezzi (LBB) or inf–sup condition needs to be satisfied. Accordingly, let:

$$\hat{u}_i^h(\mathbf{x}) = \phi^T(\mathbf{x}) U_i, \quad v_i^h = V_i^T \phi(\mathbf{x}), \quad \mathbf{x} \in \Omega \quad (23)$$

and

$$\hat{\xi}_i^h(\mathbf{x}) = \psi^T(\mathbf{x}) \Xi_i, \quad \zeta_i^h(\mathbf{x}) = Z_i^T \psi(\mathbf{x}), \quad \mathbf{x} \in \gamma_h, \quad (24)$$

where the subscripts  $i = 1, 2$  denote Cartesian components

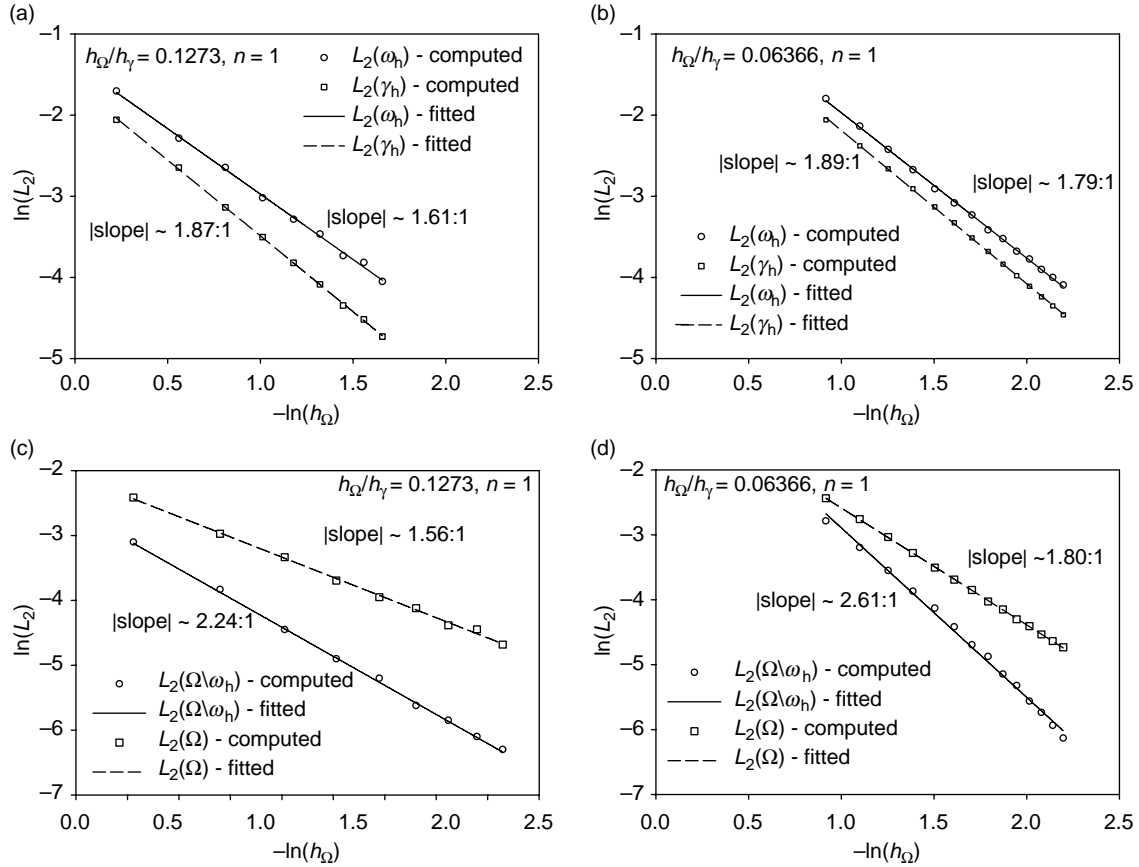


Figure 11. (a) and (b):  $L_2$  errors for  $\hat{u}$  in the interior  $\omega_h$  and on the boundary  $\gamma_h$ ; (c) and (d):  $L_2$  errors for  $\hat{u}$  in the exterior  $\Omega \setminus \omega_h$ ; simultaneous refinement in  $h_\Omega$  and  $h_\gamma$ .

of the corresponding vectors and a superscript  $h$  denotes an approximant of the subtended quantity. A subscript  $h$  denotes geometric approximation of the corresponding entity. We note though that, due to the background grid's regular structure,  $\Omega \equiv \Omega_h$ , and that  $\gamma_h$  is a non-conforming discretisation of  $\gamma$ . Moreover,  $\gamma_h$  is not necessarily constructed by matching the segments of  $\gamma_h$  with the intersections of  $\gamma$  with the background grid (Figure 9).

In the above equations,  $\mathbf{U}$  and  $\Xi$  denote vectors of nodal displacements in the background grid  $\Omega$  and of the Lagrange multipliers on the foreground grid  $\gamma_h$ , respectively. To satisfy the LBB condition, if in (23)  $\phi$  is chosen to be piecewise linear (quadratic), then  $\psi$  in (24) needs to be piecewise constant (linear). With the approximations (23) and (24), the saddle-point problems (20) and (21), upon discretisation, leads to the following (indefinite) algebraic

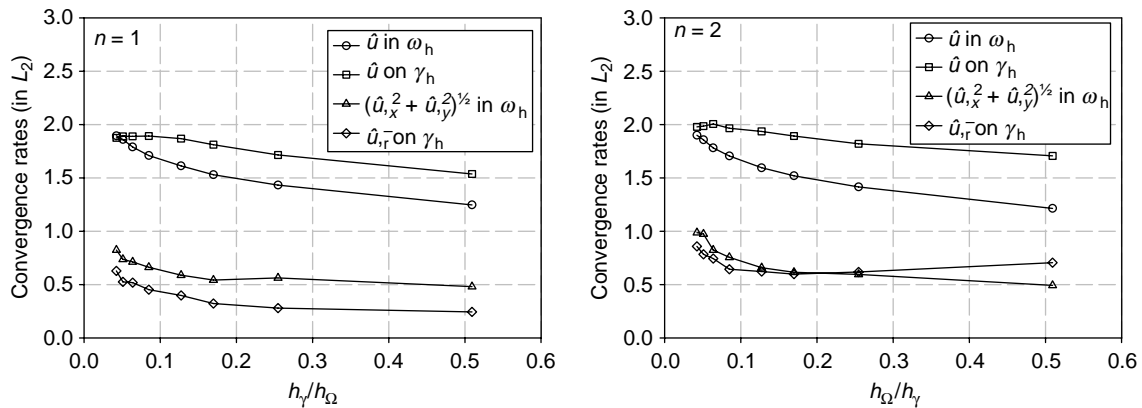


Figure 12. Convergence rates in  $L_2$ ; simultaneous refinement; various ratios  $h_\Omega/h_\gamma$ .



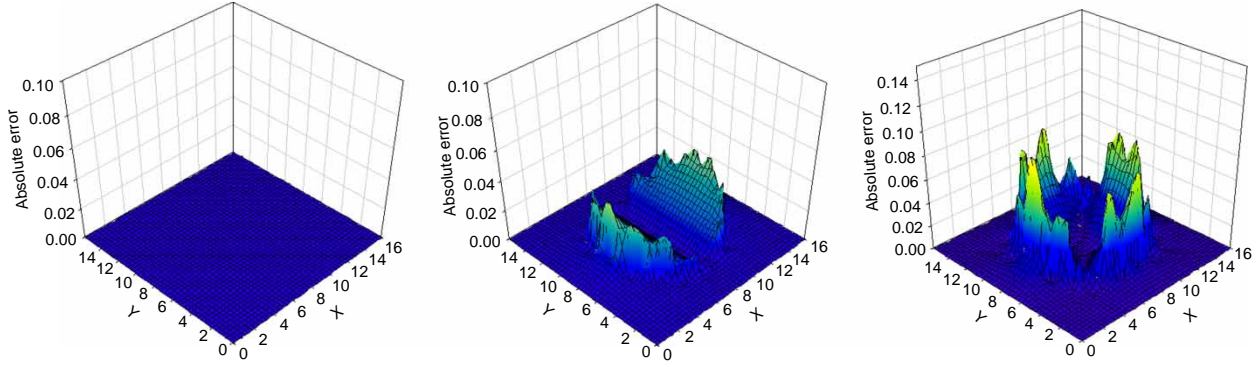


Figure 13. Absolute errors for the Laplace prototype problem; from left to right  $n = 0, 1, 2$ .

system:

$$\begin{bmatrix} \mathbf{K} & \mathbf{B}^T \\ \mathbf{B} & \mathbf{0} \end{bmatrix} \begin{bmatrix} \mathbf{U} \\ \Xi \end{bmatrix} = \begin{bmatrix} \mathbf{Q} \\ \mathbf{G} \end{bmatrix}, \quad (25)$$

where  $\mathbf{K}$  is the standard stiffness matrix arising in 2D elastostatics given by

$$\mathbf{K} = \begin{bmatrix} \mathbf{K}^{11} & \mathbf{K}^{12} \\ \mathbf{K}^{21} & \mathbf{K}^{22} \end{bmatrix},$$

with

$$\begin{aligned} \mathbf{K}_{ij}^{11} &= \int_{\Omega} \left[ (\lambda + 2\mu) \frac{\partial \phi_i}{\partial x_1} \frac{\partial \phi_j}{\partial x_1} + \mu \frac{\partial \phi_i}{\partial x_2} \frac{\partial \phi_j}{\partial x_2} \right] d\Omega, \\ \mathbf{K}_{ij}^{12} &= \int_{\Omega} \left[ \lambda \frac{\partial \phi_i}{\partial x_1} \frac{\partial \phi_j}{\partial x_2} + \mu \frac{\partial \phi_i}{\partial x_2} \frac{\partial \phi_j}{\partial x_1} \right] d\Omega, \\ \mathbf{K}^{21} &= (\mathbf{K}^{12})^T, \\ \mathbf{K}_{ij}^{22} &= \int_{\Omega} \left[ (\lambda + 2\mu) \frac{\partial \phi_i}{\partial x_2} \frac{\partial \phi_j}{\partial x_2} + \mu \frac{\partial \phi_i}{\partial x_1} \frac{\partial \phi_j}{\partial x_1} \right] d\Omega. \end{aligned} \quad (26)$$

Similarly, the constraint matrix  $\mathbf{B}$  is given by:

$$\mathbf{B} = \begin{bmatrix} \mathbf{B}^{11} & \mathbf{0} \\ \mathbf{0} & \mathbf{B}^{22} \end{bmatrix},$$

with

$$\mathbf{B}_{ij}^{11} = \mathbf{B}_{ij}^{22} = \int_{\gamma_h} \psi_i \phi_j d\gamma_h. \quad (27)$$

Furthermore, in (25)  $\mathbf{Q}$  is the vector of body forces, and  $\mathbf{G}$  is the discrete form of the right-hand side of (21). Notice that, whereas  $\mathbf{K}$  is a square matrix,  $\mathbf{B}$ , in general, is a rectangular matrix. For example, let  $n$  denote the number of grid points in  $\Omega$  and let us assume that bilinear approximations are used for  $\hat{\mathbf{u}}$ ; then  $\mathbf{K}$  will be of size

$2n \times 2n$ . Furthermore, let  $m$  denote the number of elements of the discretisation of  $\gamma$ ; to satisfy the LBB condition, we use constant approximations for the Lagrange multipliers  $\hat{\xi}$  on  $\gamma$ , and thus  $\mathbf{B}$  will be of size  $2m \times 2n$ . Of course,  $\mathbf{B}$  is highly sparse, for its elements are only non-zero for those background grid cells that are intersected by  $\gamma_h$  (Figure 6). Loosely stated and as depicted in the right column of Figure 6,  $\mathbf{B}$  is responsible for distributing the jump of the tractions on  $\gamma_h$  to the background grid of  $\Omega$ . We remark that given the regular structure of the background grid, the storage requirements for  $\mathbf{K}$  can be minimised, because it is necessary to store only a stencil (even for inhomogeneous domains), appropriately scaled by the material parameters ( $\lambda$  and  $\mu$ ).

We also note that system (25) is somewhat larger than the system that would have resulted from an unstructured discretisation of similar density if a conventional finite element approach were used. The larger size is due to two factors: (a) the Lagrange multipliers  $\Xi$  add to the displacement unknowns; their number, however, is far smaller than the number of displacement unknowns, and the latter will still control the overall size; and (b) part of

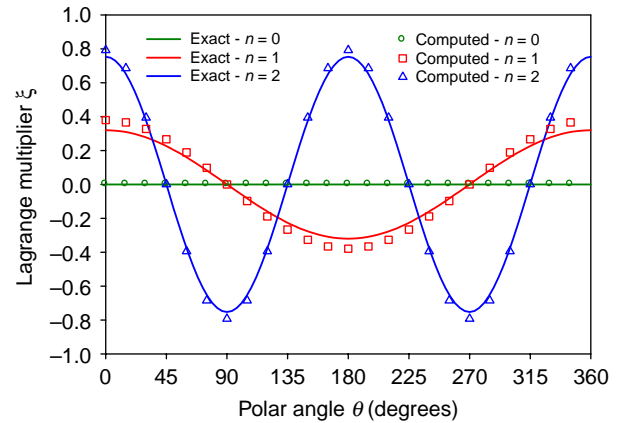


Figure 14. Exact and approximate traces of the Lagrange multipliers  $\hat{\xi}$  (33) for  $n = 0, 1, 2$  (Laplace prototype problem); approximate solution obtained for  $h_\gamma/h_\Omega = 11.78$ .

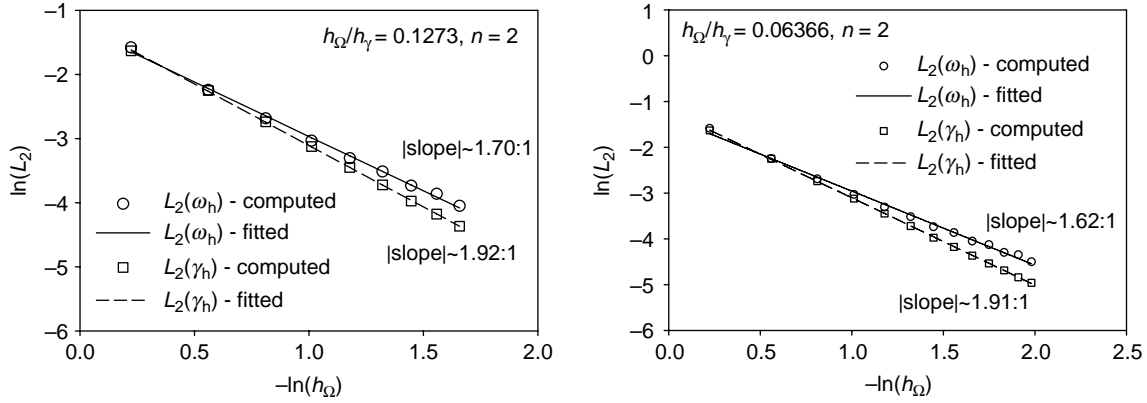


Figure 15.  $L_2$  errors for simultaneous refinement in  $h_\Omega$  and  $h_\gamma$ .

the domain that is meshed using the fictitious domain method need not be meshed with a conventional unstructured method. However, we note that the additional unknowns do not increase substantially the total system size, and, more importantly, the regular structure of the fictitious domain grid (and that of  $\mathbf{K}$  in (25)) affords the use of fast solvers, which endow the fictitious domain method with a competitive advantage over the unstructured-grid finite element approach in terms of computational cost.

#### 4. Numerical results

We conducted numerical experiments with the discrete saddle-point problem (25) for a variety of problems: here we discuss the convergence rates we observed for two prototype problems involving materially homogeneous domains – an elasticity problem and a similarly casted Laplace problem. At the end of this section, we report numerical results for the original press-fit problem, which motivated this analysis, using actual patient CT-scan data (arbitrarily heterogeneous).

##### 4.1 Prototype problems

To fix ideas, we consider first the following Laplace problem (Figure 7):

$$\Delta \hat{u}(x, y) = 0, (x, y) \in \Omega, \quad (28)$$

$$\hat{u}(x, y) = \cos n\theta, (x, y) \in \gamma, \quad (29)$$

$$\hat{u}(x, y) = \frac{5^n}{5^{2n} + 20^{2n}} \left[ (x^2 + y^2)^{n/2} + \frac{20^{2n}}{(x^2 + y^2)^{n/2}} \right] \cos n\theta, \quad (30)$$

$$(x, y) \in \Gamma,$$

where  $\theta = \arctan(y/x)$ ,  $\Omega$  is the square  $(0,16) \times (0,16)$  bounded by  $\Gamma$  and  $\omega$  is the circular domain bounded by  $\gamma$

for which  $x^2 + y^2 \leq 5^2$ . Then, the exact solution for (28)–(30) is given as

$$\hat{u}(x, y) \equiv u(x, y) = \frac{1}{5^n} (x^2 + y^2)^{n/2} \cos n\theta, \quad (31)$$

$$\text{for } 0 \leq \sqrt{x^2 + y^2} \leq 5,$$

$$\hat{u}(x, y) = \frac{5^n}{5^{2n} + 20^{2n}} \left[ (x^2 + y^2)^{n/2} + \frac{20^{2n}}{(x^2 + y^2)^{n/2}} \right] \cos n\theta, \quad (32)$$

elsewhere.

Furthermore, the exact solution for the Lagrange multipliers (jump in the radial derivative of  $u$ ) on the circular boundary  $\gamma$  is

$$\hat{\xi} = \frac{2n}{5} \frac{20^{2n}}{5^{2n} + 20^{2n}} \cos n\theta. \quad (33)$$

Problems (28)–(30) are convenient, because by controlling the value of  $n$  we can create either a smooth problem

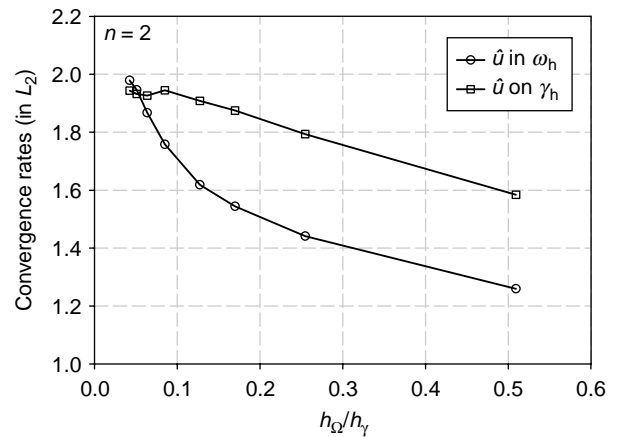


Figure 16. Convergence rates in  $L_2$  (prototype elasticity problem); simultaneous refinement; various ratios  $h_\Omega/h_\gamma$ .

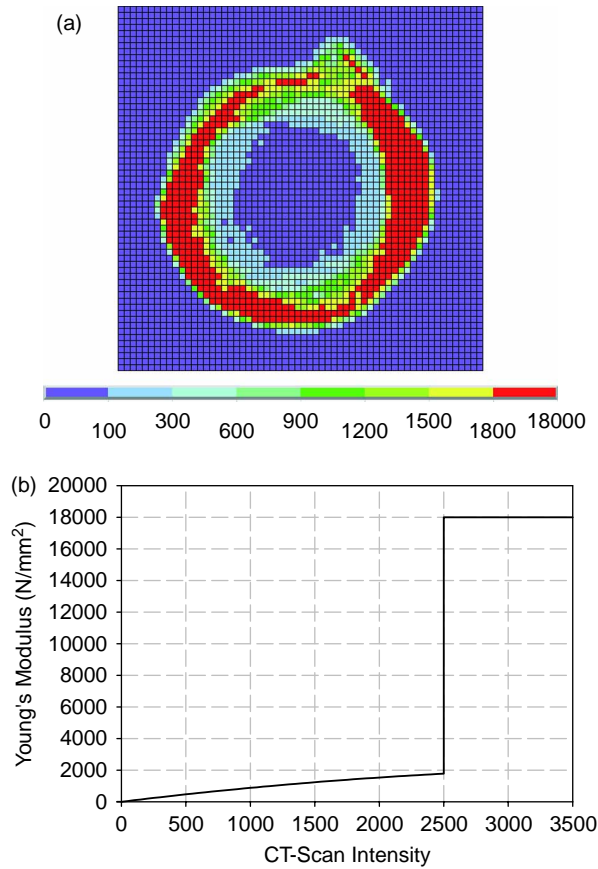


Figure 17. (a) Distribution of Young's modulus for the CT-scan of Figure 4; (b) Young's modulus to scan intensity correlation.

(for  $n = 0$ ,  $\hat{\xi} = 0$ ) or one where there will be a jump in the normal derivatives across  $\gamma$ . The presence of a jump is critical to the stability of the solution and the convergence rates. The exact solution for different values of  $n$  is depicted in Figure 8, whereas the exact solution for the Lagrange multipliers, for the same range of  $n$ , is shown in Figure 14. We remark that for  $n = 1, 2$ ,  $u \in H^2(\omega)$ , whereas  $\hat{u} \in H^{(3/2)-\epsilon}(\Omega)$ . We study first, numerically, the convergence rates in the  $L_2$  norm for the solution within the inner domain  $\omega_h$  and on the boundary  $\gamma_h$ . We use isoparametric bilinear elements for the test and trial functions of the background grid ( $\Omega_h \equiv \Omega$ ), and constant elements for the test and trial functions of the foreground grid ( $\gamma_h$ ). We use square-shaped elements for the background grid and straight-line elements for the discretisation  $\gamma_h$  of  $\gamma$ . We denote with  $h_\Omega$  the mesh metric for the background grid in  $\Omega$ , and with  $h_\gamma$  the mesh metric of  $\gamma_h$  (Figure 5). Since the mesh is common for both  $\Omega$  and  $\omega$ , the associated element size  $h_\omega = h_\Omega$ .

Figure 10 shows the  $L_2$  errors for values of the  $h_\Omega/h_\gamma$  ratio ranging from 0.045 to 0.625 (Figure 10(a,c)), and from 0.333 to 1.429 (Figure 10(b,d)), respectively. For the error calculations shown in these figures, the foreground

grid mesh is kept constant ( $h_\gamma = 2.618$  in Figure 10(a,c) and  $h_\gamma = 0.436$  in Figure 10(b,d)), whereas the background grid is refined; the small circles and squares represent computed errors, whereas the solid/dashed lines represent best fits to the computed norms. To compute the reported errors, we use the background grid solution for grid cells fully contained within  $\omega_h$ ; for grid cells intersected by the straight-line approximation to the curved boundary ( $\gamma_h$ ), we triangularise the polygon resulting from the intersections, as per Figure 9. In this figure, shaded areas represent the integration domain for such a 'boundary' cell; within each triangle we use a Gauss quadrature rule and obtain the solution at the integration points using the shape functions (bilinear) of the background grid cell and the nodal values at its vertices. In this way, the solution on boundary cells is clearly influenced by nodes exterior to  $\gamma_h$ , as it should.

Notice that the convergence rates in Figure 10 are clearly suboptimal,<sup>4</sup> for both the coarser foreground grid of Figure 10(a,c) and for the finer grid of Figure 10(b,d). Moreover, as it can be seen from Figure 10(b,d), for ratios  $h_\Omega/h_\gamma$  greater than approximately  $(1/2)(-\ln(h_\Omega)) < 1.52$ , there is no clear convergence pattern; this, numerically evaluated, critical value of the mesh metric ratio represents a stability limit. In the literature, tight estimates of the stability limit have only scantily been reported: for example, in Girault and Glowinski (1995), for the inf-sup condition to be satisfied, the stability limit was shown to be equal to  $1/3$ , for a linear-constant pair (linear triangles were used in Girault and Glowinski (1995) for the background grid). On the other hand, as reported in (Glowinski et al. 1994a), stable results were obtained using  $h_\Omega/h_\gamma \approx 2/3$ .

By contrast, when we simultaneously refine both grids, while respecting the stability limit, i.e. when  $h_\Omega/h_\gamma < 1/2$ , the convergence rates improve dramatically, as shown in Figure 11, for two different fixed ratios of  $h_\Omega/h_\gamma$ . This suggests that both background and foreground grids need to be refined simultaneously, i.e.

$$\frac{h_\Omega}{h_\gamma} \rightarrow 0, \text{ as } h_\Omega \rightarrow 0, h_\gamma \rightarrow 0. \quad (34)$$

The observed convergence rates are summarised in Figure 12 for the Laplace prototype problem and for two values of the harmonic parameter  $n$ . Notice that for fine discretisations, the solution  $u \equiv \hat{u}|_\omega$  or  $u \equiv \hat{u}|_\gamma$  in the  $L_2$  norm is  $O(h_\Omega^2)$  (consistent with the performance reported in Glowinski et al. (1994a)). Shown in the same figures are the rates associated with the first-order derivatives  $(\hat{u}_{,x}, \hat{u}_{,y}, \hat{u}_{,\gamma^-})$ , which, as expected, drop by one order to  $O(h_\Omega)$ .

We remark that in the presented numerical experiments, the errors are mostly concentrated in the interior region  $\omega$  (solutions with the exterior region  $\Omega \setminus \omega_h$  are

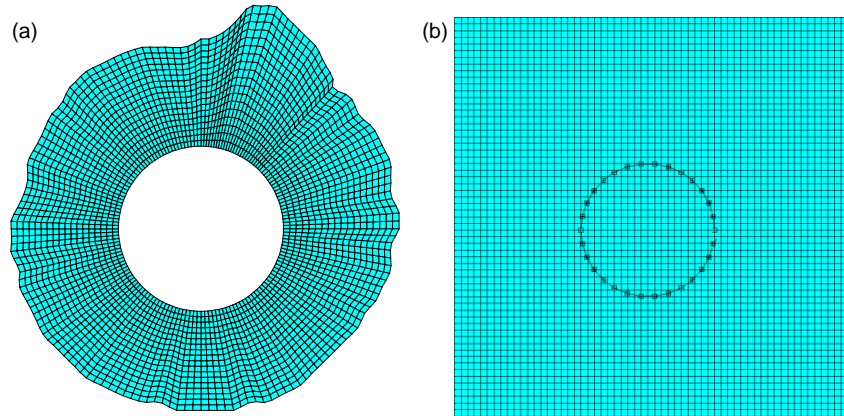


Figure 18. (a) Geometry-conforming FEM grid; (b) regular fictitious domain grid.

clearly superior to those of the interior  $\omega_h$ ); very little is contributed to the global error norms  $L_2(\Omega)$  from the exterior region; we attribute this to the closeness of the exterior Dirichlet boundary. Figure 13 pictorially depicts the absolute errors, which are concentrated on and to the interior of  $\gamma_h$ ; notice that for the smooth problem ( $n = 0$ ), for which there is no jump in the normal derivatives across  $\gamma$  ( $\hat{\xi} = 0$ ), there is no error (the exact solution is linear).

Figure 14 depicts the quite satisfactory approximation of the Lagrange multipliers by the computed solution for a single case of  $h_\Omega/h_\gamma$ . We note that although the approximate Lagrange multipliers reside on  $\gamma_h$ , the exact ones reside on  $\gamma$ . To compute the error, we integrate over  $\gamma_h$ ; the approximate Lagrange multipliers are readily available. For the exact solution, we project each integration point onto  $\gamma$  based on the associated polar

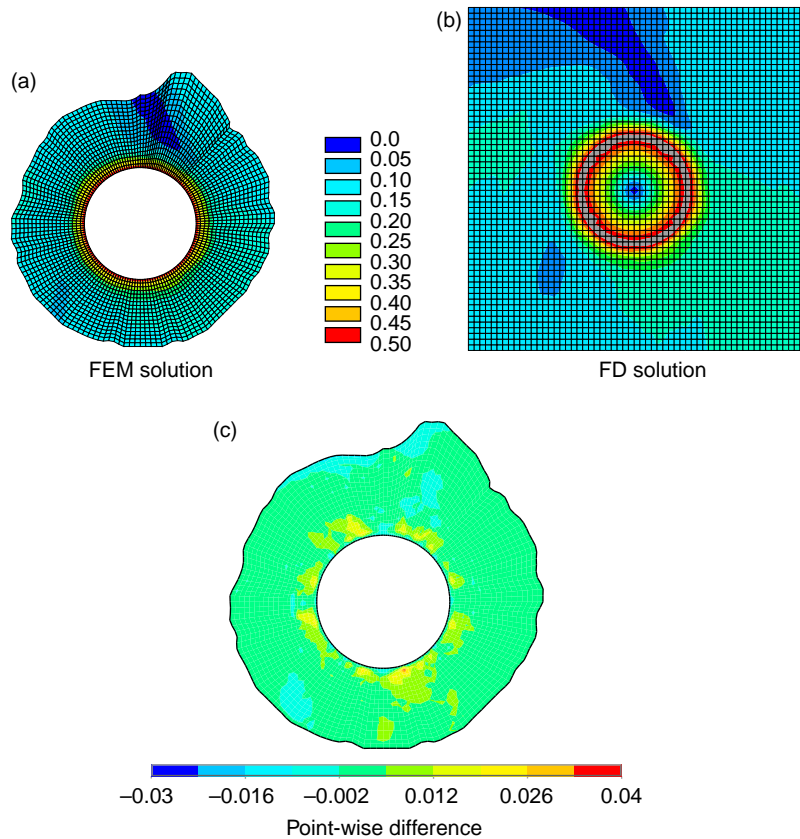


Figure 19. (a) and (b): Total displacement distribution; press-fit amount 0.5 mm; (c) distribution of total displacement difference between FEM and fictitious domain; scale in mm.

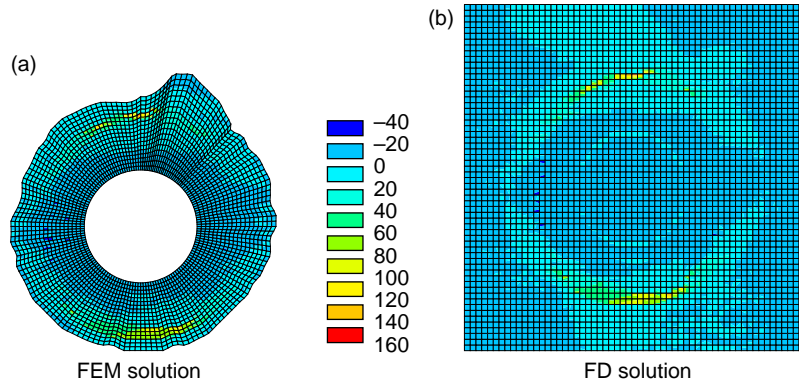


Figure 20. Distribution of  $\sigma_{xx}$  stresses; scale in  $\text{N/mm}^2$ .

angle and compute the corresponding exact multiplier at the projected location of  $\gamma$ . This is not mathematically rigorous, but provides a reasonable approach to assess the accuracy of the multipliers. Moreover, we remark that the convergence rates similar to the ones we discuss here also hold for the 3D counterparts of the prototype problems (Biros et al. 1997).

We turn next to a prototype elasticity problem similar to (28)–(30). Referring again to Figure 7, we seek to find the Cartesian components  $\hat{u}_x, \hat{u}_y$  of the displacement vector such that

$$\text{div } \hat{\boldsymbol{\sigma}}(x, y) = 0, \quad (x, y) \in \Omega, \quad (35)$$

$$\hat{u}_x(x, y) = \cos n\theta, \hat{u}_y(x, y) = -\sin n\theta, \quad (x, y) \in \gamma, \quad (36)$$

$$\begin{aligned} \hat{u}_x(x, y) = & \left[ c_1(x^2 + y^2)^{(n-1)/2} + c_2(x^2 + y^2)^{(n+1)/2} \right. \\ & \left. + c_3(x^2 + y^2)^{-(n+1)/2} + c_4(x^2 + y^2)^{-(n-1)/2} \right] \\ & \cos n\theta, \quad (x, y) \in \Gamma, \end{aligned} \quad (37)$$

$$\begin{aligned} \hat{u}_y(x, y) = & \left[ -c_1(x^2 + y^2)^{(n-1)/2} - c_2 \frac{n(\lambda + \mu) + 2(\lambda + 2\mu)}{n(\lambda + \mu) - 2\mu} \right. \\ & \left. (x^2 + y^2)^{(n+1)/2} + c_3(x^2 + y^2)^{-(n+1)/2} \right. \\ & \left. + c_4 \frac{n(\lambda + \mu) - 2(\lambda + 2\mu)}{n(\lambda + \mu) + 2\mu} (x^2 + y^2)^{-(n-1)/2} \right] \\ & \sin n\theta, \quad (x, y) \in \Gamma, \end{aligned} \quad (38)$$

where  $\theta = \arctan(y/x)$ ,  $n \geq 2$  and  $c_1, c_2, c_3, c_4$  are appropriate constants. The constants were obtained by solving an auxiliary Dirichlet problem in the annular region defined by the inner ( $\gamma$ ) and outer circles shown in Figure 7, respectively, by setting the conditions on the outer circle to

be  $\hat{u}_x = (1/2)\cos n\theta$ ,  $\hat{u}_y = -(1/2)\sin n\theta$ . The boundary conditions on  $\Gamma$  were obtained as the restriction on  $\Gamma$  of the solution within the annular region.<sup>5</sup> With these definitions, the exact solution within  $\omega$  becomes

$$\begin{aligned} \hat{u}_x(x, y) &= \left[ \frac{(x^2 + y^2)^{1/2}}{5} \right]^{n-1} \cos n\theta, \\ \hat{u}_y(x, y) &= - \left[ \frac{(x^2 + y^2)^{1/2}}{5} \right]^{n-1} \sin n\theta, \end{aligned} \quad (39)$$

whereas within  $\Omega \setminus \omega$  it is given by (35) and (36). As it can be seen from Figures 15 and 16, the observations made about the Laplace problem are true here as well (both problems are elliptic). Figure 15 shows the convergence rates for the displacement solution on  $\gamma$  and in  $\omega$  under simultaneous refinement with fixed ratio, whereas Figure 16 shows the cumulative rates that clearly approach  $O(h_\Omega^2)$  as  $(h_\Omega/h_\gamma) \rightarrow 0$ .

#### 4.2 Press-fit problem over an inhomogeneous region

Next, we consider the original press-fit problem. Shown in Figure 4 is, in grey-scale, an actual adult patient CT-scan of a femoral slice; the dimensions of the square region depicted in Figure 4 are 48 mm  $\times$  48 mm. The red inset represents the circular cross section of a rigid implant of radius 8 mm. We considered a (typical) press-fit amount of 0.5 mm that was applied as a Dirichlet condition in the radial direction on  $\gamma$ , whereas the outer boundary  $\Gamma$  of the slice was taken to be traction-free.

To solve the resulting boundary-value problem, we used published correlations (Mow and Hayes 1997) between experimentally obtained values for Young's modulus and the CT-scan intensity, to create the material map shown in Figure 17(a); Poisson's ratio was assumed constant at 1/3. In this map, the red regions correspond to higher values of Young's modulus, with the highest amongst them corresponding to the cortical part (exterior) of the bone. The lighter pixels between the red and blue

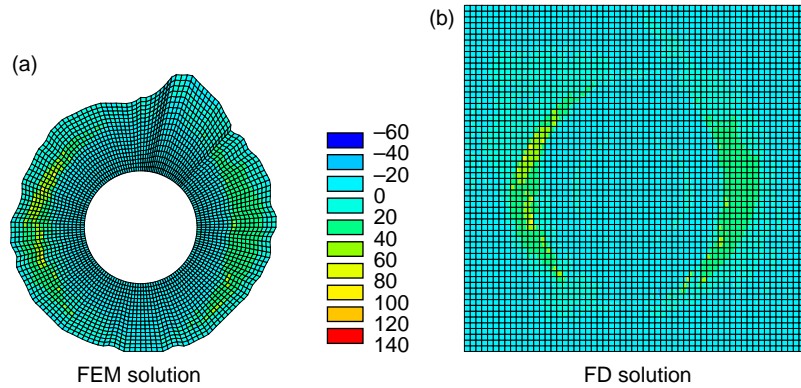


Figure 21. Distribution of  $\sigma_{yy}$  stresses; scale in  $\text{N/mm}^2$ .

regions at the outer fibres of the cortical bone are image artefacts. Shown in Figure 17(b) is the corresponding curve we used for Young's modulus.

We used both a finite-element approach based on a geometry-conforming mesh (Figure 18(a)) and the fictitious domain method to solve the press-fit problem. The solid model used in the geometry-conforming mesh case was obtained by manually delineating the outer boundary of the femur. For the fictitious domain grid, (Figure 18(b)), the material properties are readily available from the CT-scan map shown in Figure 17(a). By contrast, for each element of the geometry-conforming grid, we use the coordinates of its barycentre to query the structured material map shown in Figure 17(a) in order to assign properties. Since there is overlap between the elements of the geometry-conforming and regular meshes, there are small differences between the material properties, and we expect these differences to manifest, especially in the stress distributions. Nevertheless, as argued in Section 1, the ground-truth data are represented by the CT-scan, and hence we hold the fictitious domain as the more faithful to the original data of the two solutions.

Shown in Figure 19 are the distributions of total displacements obtained using the meshes depicted in Figure 18. Although, visually, both solutions appear close, Figure 19(c) shows the point-wise difference distribution; notice that the larger differences are close to the inner boundary. For example, the highest recorded difference was 0.04 corresponding to a displacement of approximately 0.5 (8% difference). Figures 20 and 21 show similar comparisons for the  $\sigma_{xx}$  and  $\sigma_{yy}$  stress components. To ease the comparison, Figure 22 shows the radial displacement and hoop stress on a circle of radius 15.5 mm that is fully embedded within the geometry-conforming mesh of Figure 18. Although the agreement between the two solutions for the displacements is excellent, differences can be seen in the stress distribution. Again, we attribute these differences, partially, to the mismatch in the underlying material properties between the two meshes. Finally, Figure 23 shows a comparison on the displacement components along the outer boundary of the geometry-conforming grid; the agreement is quite satisfactory. Lastly, we note that the unstructured finite element grid comprised 3021 nodes, whereas the fictitious

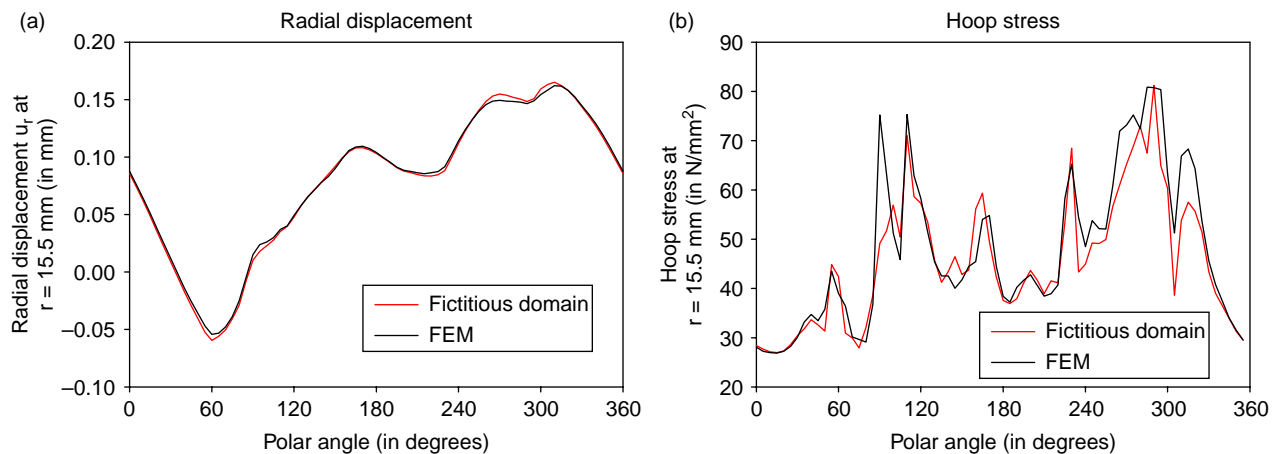


Figure 22. Comparisons of radial displacement component and hoop stress along a circle at  $r = 15.5$  mm.

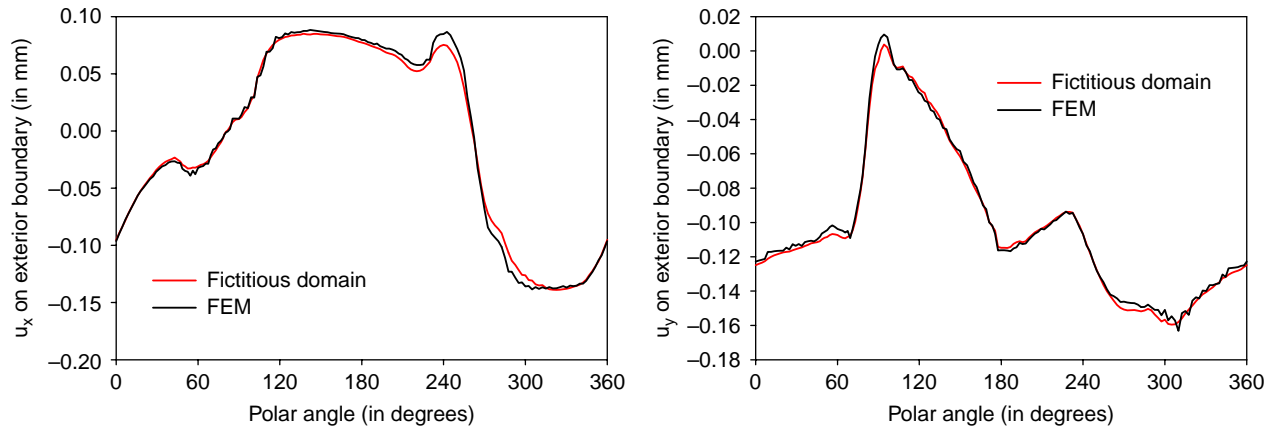


Figure 23. Comparisons of displacement components on the delineated exterior boundary.

domain regular grid had 3721 nodes, and the press-fit boundary was discretised using 73 nodes. We used direct solvers for both approaches, resulting in comparable solution times.

## 5. Conclusions

In this article, motivated by the needs of patient-specific modelling arising in computer-assisted orthopaedic surgery, we presented a methodology for tackling problems for which the material profile originates from medical imaging data that are typically delivered on regular grids. For such problems, the fictitious domain method is a natural choice, because it avoids the segmentation, surface reconstruction and meshing phases required by unstructured geometry-conforming simulation methods. Using prototype problems, we presented numerical results that exhibit optimal convergence rates in the domain of interest. Similarly, satisfactory results were presented using actual patient CT-data for the press-fit problem arising in the cementless implantation in total-hip replacement surgeries.

## Acknowledgement

We are grateful for the partial support for the research reported herein provided by the National Science Foundation under grant awards IIS-9422734 and ATM-0326449.

## Notes

1. Bone typically regenerates and in many cases will grow into the porous surface of an implant; such long-term post-operative bone 'remodelling' processes are not taken into account in the analysis of the short-term intra-surgical processes presented herein.
2. The cortical bone's behaviour is closer to an orthotropic material; here we opted for isotropic linear elastic behaviour

for simplicity, even though the presented methodology is not limited by the particular form of the constitutive relation.

3. We will henceforth refer to traction jump  $\xi$  as the Lagrange multipliers.
4. For the bilinear-constant pair, we use the term optimal to refer to  $O(h_\Omega^2)$  rates.
5. The expressions for the constants are quite lengthy and are thus not included here; however, they can be readily obtained using any symbolic computation software package.

## References

- Astrakhtantsev GP. 1978. Methods of fictitious domains for a second-order elliptic equation with natural boundary conditions. *USSR Comput Math Math Phys.* 18:114–121.
- Baaijens FPT. 2001. A fictitious domain-mortar element method for fluid–structure interaction. *Internat J Numer Methods Fluids.* 35:743–761.
- Babuška I. 1973. The finite element method with Lagrange multipliers. *Numerische Mathematik.* 16:179–192.
- Biros G, Kallivokas LF, Ghattas O, Jaramaz B. 1997. Direct CT-scan to finite element modeling using a 3D fictitious domain method with an application to biomechanics. *Proceedings Fourth US National Congress on Computational Mechanics; San Francisco, CA.* p. 404.
- Collino F, Joly P, Millot F. 1997. Fictitious domain method for unsteady problems. *J Comput Phys.* 138:907–938.
- De Hart J, Peter GWM, Schreurs PJG, Baaijens FPT. 2000. A two-dimensional fluid–structure interaction model of the aortic valve. *J Biomech.* 33:1079–1088.
- De Hart J, Peter GWM, Schreurs PJG, Baaijens FPT. 2003. A three-dimensional computational analysis of fluid–structure interaction in the aortic valve. *J Biomech.* 36:103–112.
- Farhat C, Hetmaniuk U. 2002. A fictitious domain decomposition method for the solution of partially axisymmetric acoustic scattering problems. Part I: Dirichlet boundary conditions. *Internat J Numer Methods Engrg.* 54:1309–1332.
- Finogenov SA, Kuznetsov YA. 1988. Two-stage fictitious components method for solving the Dirichlet boundary value problem. *Sov J Numer Anal Math Modelling.* 3:301–323.
- Fix GM. 1976. Hybrid finite element methods. *SIAM Rev.* 18(3):460–484.

- Girault V, Glowinski R. 1995. Error analysis of a fictitious domain method applied to a Dirichlet problem. *Japan J Indust Appl Math.* 12:487–514.
- Glowinski R. 2003. Fictitious domain methods for incompressible viscous flow: application to particulate flow. In: Ciarlet PG, Lions JL, editors. *Handbook of numerical analysis.* Vol. IX:619–769. Amsterdam: North-Holland.
- Glowinski R, Kuznetsov YA. 1998. On the solution of the Dirichlet problem for linear elliptic operators by a distributed Lagrange multiplier method. *CR Acad Sci Paris.* 1:693–698.
- Glowinski R, Pan T-W, Hesla TI, Joseph DD, Periaux J. 2001. A fictitious domain approach to the direct numerical simulation of incompressible viscous flow past moving rigid bodies: application to particulate flow. *J Comput Phys.* 169:363–426.
- Glowinski R, Pan T-W, Periaux J. 1994a. A fictitious domain method for Dirichlet problem and applications. *Comput Methods Appl Mech Engrg.* 111:283–303.
- Glowinski R, Pan T-W, Periaux J. 1994b. A fictitious domain method for external incompressible viscous flow modeled by Navier–Stokes equations. *Comput Methods Appl Mech Engrg.* 112:133–148.
- Glowinski R, Pan T-W, Periaux J. 1997. A Lagrange multiplier-fictitious domain method for the numerical simulation of incompressible viscous flow around moving rigid bodies. *Math Probl Mech.* 1:361–369.
- Glowinski R, Pan T-W, Periaux J. 1998. Distributed Lagrange multiplier methods for incompressible viscous flow around moving rigid bodies. *Comput Methods Appl Mech Engrg.* 151:181–194.
- Glowinski R, Pan T-W, Wells RO, Zhou X. 1996. Wavelet and finite element solutions for the Neumann problem using fictitious domains. *J Comput Phys.* 126:40–51.
- Heikkola E, Kuznetsov YA, Neittaanmaki P, Toivanen J. 1998. Fictitious domain methods for the numerical solution of two-dimensional scattering problems. *J Comput Phys.* 145:89–109.
- Heikkola E, Rossi T, Toivanen J. 2003. A parallel fictitious domain method for the three-dimensional Helmholtz equation. *SIAM J Sci Comput.* 5:1567–1588.
- Hetmaniuk U, Farhat C. 2003a. A fictitious domain decomposition method for the solution of partially axisymmetric acoustic scattering problems. Part 2: Neumann boundary conditions. *Internat J Numer Methods Engrg.* 58:63–81.
- Hetmaniuk U, Farhat C. 2003b. A finite element-based fictitious domain decomposition method for the fast solution of partially axisymmetric sound-hard acoustic scattering problems. *Finite Elem Anal Des.* 39:707–725.
- Kallivokas LF, Jaramaz B, Ghattas O, Shah S, DiGioia AM. 1996. Biomechanics-based pre-operative planning in THR – application of fictitious domain method. In: *Advances in bioengineering.* ASME Winter Annual Meeting; Atlanta, GA, BED-Vol. 33. p. 389–390.
- Kanade T, DiGioia AM, Ghattas O, Jaramaz B, Blackwell M, Kallivokas LF, Morgan F, Shah S, Simon DA. 1996. Simulation, planning, and execution of computer-assisted surgery. *Proceedings of the NSF Grand Challenges Workshop, Washington, DC.*
- Krejčí R, Bartoš M, Dvořák J, Nedoma J, Stehlik J. 1997. 2D and 2D finite element pre- and post-processing in orthopaedy. *Internat J Med Inform.* 45:83–89.
- Lengsfeld M, Schmitt J, Alter P, Kaminsky J, Leppek R. 1998. Comparison of geometry-based and CT voxel-based finite element modelling and experimental validation. *Med Eng Phys.* 20:515–522.
- Maitre JF, Tomas L. 1999. A fictitious domain method for Dirichlet problems using mixed finite elements. *Appl Math Lett.* 12:117–120.
- Mow VC, Hayes WC. 1997. *Basic orthopaedic biomechanics.* 2nd ed. New York: Lippincott-Raven Publishers.
- Na S-W, Kallivokas LF, Jaramaz B. 2002. Modeling of a press-fit problem in computational biomechanics using the fictitious domain method. *Proceedings 14th US National Congress on Theoretical and Applied Mechanics; Blacksburg, VA.* p. 313.
- Nasir HM, Kako T, Koyama D. 2003. A mixed-type finite element approximation for radiation problems using fictitious domain method. *J Comput Appl Math.* 152:377–392.
- Patankar NA, Singh P, Joseph DD, Glowinski R, Pan T-W. 2000. A new formulation of the distributed Lagrange multiplier-fictitious domain method for particulate flows. *Internat J Multiphase Flow.* 26:1509–1524.
- Saul'ev VK. 1963. On solution of some boundary value problems on high performance computers by fictitious domain method. *Sib Math J.* 4:912–925.
- Shah S, Kallivokas LF, Jaramaz B, Ghattas O, DiGioia AM. 1995. The fictitious domain method for biomechanical modeling using patient-specific data: promise and prospects. *Proceedings of the Second International Symposium on Medical Robotics and Computer Assisted Surgery; Baltimore, MD.* p. 329–333.